Impact of impurities on the fabrication and performances of yttrium-doped thoria electrolyte ceramics

Nicolas Clavier, Yanis Cherkaski, Laurent Brissonneau, Nicolas Dacheux

Impact of impurities on the fabrication and performances of yttrium-doped thoria electrolyte ceramics

N. Clavier [1,], Y. Cherkaski [1,2], L. Brissonneau [2], N. Dacheux [1]*

[1] ICSM, Univ Montpellier, CEA, CNRS, ENSCM, Bagnols/Cèze, France

[2] CEA, DES, IRESNE, DTN, SMTA, LMCT, Site de Cadarache, 13108 St-Paul lez Durance, France

*** Corresponding author:**

Dr. Nicolas CLAVIER
ICSM, Univ Montpellier, CEA, CNRS, ENSCM,
Site de Marcoule
BP 17171
30207 Bagnols sur Cèze
France

Phone : + 33 4 66 33 92 08
Fax : + 33 4 66 79 76 11

nicolas.clavier@icsm.fr

Abstract :

The effect of several impuritites on the life-cycle of yttria-doped thoria electrolyte was evaluated in this study. All the oxide exhibited the single-phase fluorite-type structure expected for such materials, while the variation of the unit cell parameter attested for the incorporation of the impurities in the lattice. Doping with 0.2 – 1 wt.% of Al, Si or Zr only slightly affected the morphology of the powders, as well as the microstructure of the pellets obtained after sintering, even if a deleterious effect, leading to the embrittlement of the samples, was observed for high silicon contents.

The presence of silicon and zirconium in the ceramic further modified its electrical properties. The grain conductivity was always found to decrease. Impedance spectroscopy also revealed a strong modification of the signal assigned to grain boundaries, which evidenced that impurities partially migrated during the sintering step. Finally, corrosion tests undertaken in liquid sodium at 773 K showed that the pellets were fragilized by the presence of silicon or high zirconium contents, possibly through the formation of Na_2MO_3 ternary oxides at the grain boundaries.

From a general point of view, silicon seems to be the most harmful impurity that should be especially checked during the fabrication processes.

Keywords : Yttrium-doped thoria ; Oxygen monitoring sensors ; Impurities ; Electrical properties ; Sodium corrosion

1. Introduction

Sodium-cooled fast reactors (SFR) are amongst the concepts envisaged for the development of the fourth generation of nuclear reactors [1]. In such units, the chemistry of the liquid sodium coolant has to be carefully controlled, especially regarding its purity in terms of oxygen content. Indeed, this latter is known to impact significantly the corrosion of the stainless steel claddings of the primary vessels. As such, it should be kept typically under a few parts per million (ppm) [2]. To operate an in-situ monitoring, the use of electrochemical sensors has been proposed for a long time. They are usually based on an internal reference (either gas or metal/oxide couple), which is separated from the liquid sodium media by a ceramic electrolyte ensuring the conduction of O^{2-} anions. As a key-component to this device, the ceramic should be thermo-mechanically resistant and compatible with sodium at high temperature (about 673 K) and purely ionic conductor [3, 4]. On this basis, several materials were tested, with a particular emphasis for yttrium-doped MO_2 oxides (with M = Zr, Hf, Ce or Th) [5].

Among these ceramics, recent works demonstrated that homogeneous $Th_{1-x}Y_xO_{2-x/2}$ solid solutions obtained by wet-chemistry methods present excellent properties, able to fulfill the requirements of an electrolyte to be used in liquid sodium at high temperature. First, they can be sintered towards high densites (typically above 97%TD) while keeping submicrometric grain size [6]. The characterization of the electrical properties by the means of impedance spectroscopy showed a maximum of conductivity between x = 0.08 and x = 0.15 (i.e. 2.8 and 5.5 wt.% in yttrium, respectively), independently from the microstructure [3, 7]. Finally, the ceramics were found to be durable during corrosion tests in liquid sodium, even for penalizing oxygen concentration up to 70-80 ppm [8]. All these results showed that yttrium-doped thoria could be an excellent candidate for oxygen sensors to be used in liquid sodium. Nevertheless, they were obtained at the lab-scale on highly pure materials that cannot be representative for real items fabricated industrially.

Indeed, these latter could contain impurities up to some hundreds ppm, that can come either from the chemicals used in the synthesis or from the preparation process. Various authors already pointed out the deleterious effect associated to impurities on the life-cycle of $M_{1-x}Y_xO_{2-x/2}$ ceramics, especially concerning their chemical durability during corrosion tests in liquid sodium [9-11]. It is then of primary importance to estimate a critical content of impurities that can be accepted to use the electrolyte ceramics in specific operating conditions. Therefore, this paper reports the effect of various impurities on the behavior of $Th_{1-x}Y_xO_{2-x/2}$ solid solutions

during preparation and sintering steps, as well as during the corrosion tests. Its impact on electrical properties will also be evaluated. In this study, three impurities have been selected to be incorporated in the ceramics, i.e. zirconium, silicon, and aluminium. Among them, silicon was frequently reported in the literature, and associated with the formation of secondary phases such as Na_2ThSiO_5 or Na_2SiO_5 [10]. Although present in a lesser extent Zr and Al were also mentioned by several authors [9, 10]. Moreover, these three element present not only different stable oxidation states (i.e. +IV for Zr and Si, +III for Al), but also distinct ionic radii for a same valency (0.8 Å for Zr (IV) vs 1.05 Å for Th (IV) in 8-fold coordinance) [12], which should impact the material performances differently. Also, the impurities contents tested herein varied from 0.2 to 1 wt.% with the aim to be representative of extreme conditions for the preparation, properties and durability of the material. As such, they should allow one to discriminate which kind of element could be harmful for the electrolyte ceramics.

2. Experimental

Preparation of the powdered samples. Thorium and yttrium nitrate salts ($Th(NO_3)_4.5H_2O$ and $Y(NO_3)_3.6H_2O$), were supplied by Ibilabs and Sigma-Aldrich, respectively, as well as oxalic acid. Purity of thorium and yttrium reactants was above 99.8% while that of oxalic acid was 99.5%. Zirconium, aluminium and silicon were obtained from SCP Science under the form of 10 $g.L^{-1}$ standard solutions prepared in 0.2M HNO_3. The synthesis protocol was based on the co-precipitation of the cations as oxalates, as already described in our previous publications [13, 14]. Briefly, thorium and yttrium nitrate salts were first dissolved in 1 M HNO_3 with a molar ratio Y/(Th+Y) = 0.15. This particular composition (i.e. $Th_{0.85}Y_{0.15}O_{1.925}$, hereafter considered as the reference sample free from impurities, and designed as pure sample) was chosen as it was generally correlated to a maximum in the ionic conductivity of the ceramic [3, 8]. Zr, Al or Si were then introduced at three different concentrations, i.e. 0.2, 0.4 and 1 wt.% with regards to the (Th+Y) content. The equivalent cationic stoichiometry of the oxide compounds prepared is supplied in **Table 1**. Similarly, some samples containing two different impurities were prepared with Al/Si or Zr/Si equal to 0.5/0.5 wt.% and 1/1 wt.%. In all the cases, the final concentration of cations in the mixture was close to 0.5 M. The resulting solutions was then poured in large excess of oxalic acid, leading to a very rapid precipitation. The precipitate was further recovered by centrifugation at 4500 rpm, then washed several times with deionized water and ethanol, and finally dried overnight at 363 K.

The precipitation yields were determined for all the cations through ICP-AES (Inductively Coupled Plasma-Atomic Emission Spectrometry) analysis of the supernatants. In good agreement with previous studies [13], the precipitation of thorium and yttrium was found to be quantitative (i.e. %yield > 99.9). Silicon and aluminium were also mostly retained in the solid phase with recovery yields higher than 95 %. Conversely, zirconium was only partly precipitated, with 20 % of Zr remaining in solution after the precipitation process. Despite these small differences, the samples are labelled as 0.2, 0.4 or 1 wt.% for simplification purposes.

Finally, oxide powders were obtained after a thermal treatment at 873 K during 4 hours under air atmosphere. These conditions were already proven to provide an efficient elimination of the carbon coming from the decomposition of the organic moieties, and a good reactivity of the final powders regarding to the sintering step [6].

Table 1. Cationic stoichiometry of the oxide samples prepared when doping with various impurities contents.

$Th_mY_xI_z$	Si	Al	Zr
0.2 wt.%	$Th_{0.837}Y_{0.148}Si_{0.015}$	$Th_{0.837}Y_{0.148}Al_{0.015}$	$Th_{0.846}Y_{0.149}Zr_{0.005}$
0.4 wt.%	$Th_{0.825}Y_{0.146}Si_{0.029}$	$Th_{0.824}Y_{0.146}Al_{0.030}$	$Th_{0.842}Y_{0.149}Zr_{0.009}$
1 wt.%	$Th_{0.790}Y_{0.139}Si_{0.071}$	$Th_{0.788}Y_{0.139}Al_{0.073}$	$Th_{0.830}Y_{0.147}Zr_{0.023}$

Powders characterization. All the samples were characterized by Powder X-Ray Diffraction (PXRD) using a Bruker D8 diffractometer equipped with a Lynxeye detector in the reflection geometry with Göbel mirror and using Cu $K\alpha_{1,2}$ radiation ($\lambda_{average}$ = 1.54184 Å). PXRD patterns were recorded at room temperature in the 5 – 100° range (2θ), a step size of $\Delta(2\theta)$ = 0.01° and a total counting time of about 1.5 hours per sample. All the PXRD patterns were refined by the Rietveld method using the Cox-Hastings pseudo-Voigt profile function [15] implemented in the Fullprof_suite program [16]. Additionally, SEM observations were carried out on the pristine samples using a FEI Quanta 200 ESEM FEG microscope equipped with a Large Field Detector (LFD) and a Back-Scattered Electron Detector (BSED). A low acceleration voltage of 5-10 kV coupled with low vacuum conditions (50 Pa water vapor) was chosen to observe the samples without any additional preparation step such as metallization. After corrosion tests in sodium, altered samples were fractured and observed using a Zeiss Evo HD 15MA microscope operating at 20 kV and equipped with a Oxford Instruments SDD X-Max 50 EDS detector.

Sintering. About 200 mg of each oxide sample were first shaped by uniaxial pressing (200 MPa) at room temperature, resulting in green pellets of 8 mm in diameter and about 1.3 mm in thickness. Dilatometric measurements were then conducted on a Setaram Setsys Evolution apparatus. For this purpose, samples were initially placed between two alumina platelets, and heated up to 1873 K under air flow, considering a heating rate of 10 $K.min^{-1}$.

Green pellets were also sintered during 8 hours at 1873 K or 1973 K in a graphite furnace (AET Technologies) under primary vacuum. These conditions were chosen as they previously allowed us to reach the specifications targeted for the ceramics, i.e. dense samples (typically with d > 96 % of the theoretical density (TD)) with a submicrometric grain size [6]. The density of the sintered samples was determined by geometrical measurements of the pellets dimensions with the help of a digital calliper.

Electrical characterizations. Electrical properties of the sintered samples were evaluated by impedance spectroscopy, using a Solartron 1260 impedancemeter between 0.1 Hz and 10 MHz. The experiments were undertaken under Ar/H_2 3 % between 623 K and 973 K to reach an dioxygen pressure $P(O_2)$ of about 10^{-30} atm. This latter value was determined from direct measurement by a GENAIR apparatus (SETNAG) at 923 K, and conversion at the operating temperature to take into account the displacement of the H_2/H_2O equilibrium. In these conditions, the ceramic samples prepared are expected to be strictly ionic conductors [17]. Additional details regarding the preparation of the samples have been described in our previous publications [8]. The Nyquist diagrams collected were fitted with the ZView software (Scribner Associates Incorporated). The numbers in the diagrams indicate the logarithm of the measuring frequency. All the measurements were double or triple checked, which led to estimate the uncertainty attached to the conductivity to about 20–30 %. This important bias is mainly linked with the difficulties encountered during the fitting procedure.

Corrosion tests. Static corrosion tests in liquid sodium were undertaken in dedicated 316L steel containers filled with 6-7 g of high purity grade sodium supplied by MSSA (Métaux Spéciaux). Prior to the corrosion experiments, the oxygen concentration was estimated to about 80 ppm, which can increase significantly the corrosion kinetics and then represents penalizing conditions for the performance of the electrolyte ceramic. Sintered pellets were inserted in a custom stainless steel device allowing the complete immersion of the ceramics in liquid sodium. This setup was placed in an oven at 773 K during 500 hours in order to perform the corrosion

tests. Afterwards, the pellets were recovered from the liquid sodium, and washed with ultra-pure ethanol before characterization [8].

3. Results and discussion

3.1 Characterization of the oxide powders

The oxide powders resulting from the calcination of the oxalate precursors were first characterized by PXRD. As an example, **Figure 1** shows all the patterns collected for Si-doped samples, while similar results were obtained for the other impurities tested (see supplementary material). Indeed, whatever the dopant and its content, the PXRD diagrams systematically exhibited the classical diffraction lines of the fluorite-type cubic structure of $Th_{0.85}Y_{0.15}O_{1.925}$ (Fm-3m space group). As such, no undesired additional phase was observed, such as SiO_2, Al_2O_3 or ZrO_2, at least within the limits of detection of the apparatus considered.

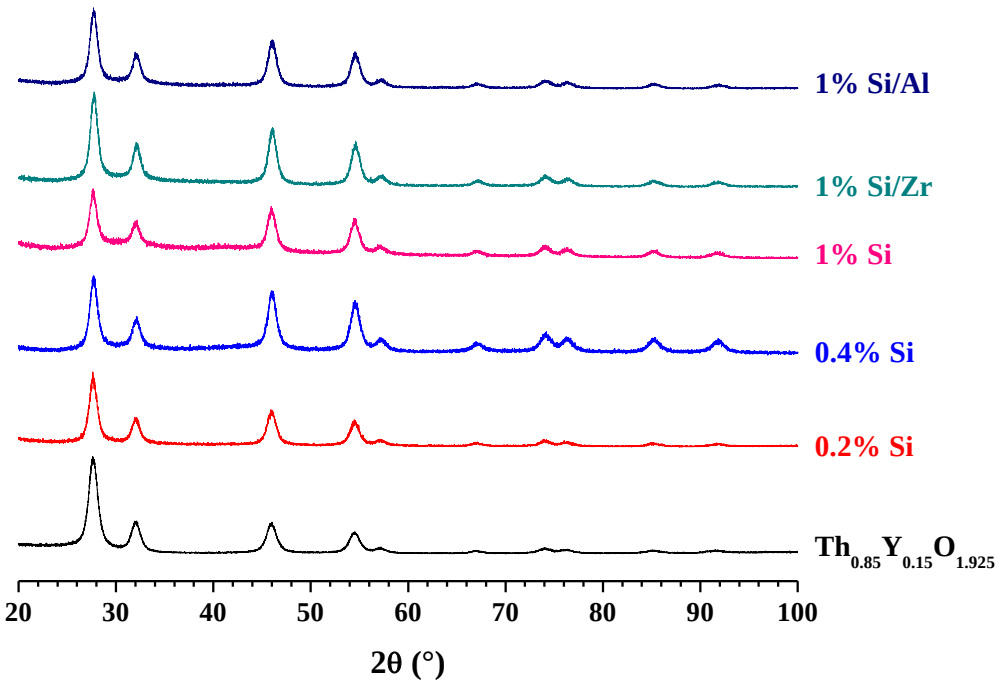

Figure 1. XRD patterns of $Th_{0.85}Y_{0.15}O_{1.925}$ doped with various amounts of silicon, aluminium and zirconium. The data collected for the pure compound are reported for comparison purposes.

The lattice parameters obtained by Rietveld refinement of the PXRD data are reported in **Table 2**. For all the impurities tested, the unit cell volume appears to be slightly above that determined for the undoped reference. This slight volume variation might be the consequence of the dopants incorporation in the lattice, either through insertion or by direct substitution on the cationic sites. However, one must keep in mind that such a small volume variation could also arise from the nanostructuration of the powders. Indeed, several authors recently showed that oxide powders coming from the thermal conversion of oxalate precursors consist of aggregates of nanometric crystallites [18-20]. In these entities, the predominance of the surface *versus* the volume generates a tensile effect on the lattice leading to higher unit cell volumes compared with bulk materials [21]. The difference in the unit cell volume observed herein then could also be assigned to the variation of the average crystallite size when doping $Th_{0.85}Y_{0.15}O_{1.925}$.

Table 2. Unit cell parameters determined by Rietveld refinement of PXRD data for $Th_{0.85}Y_{0.15}O_{1.925}$ samples doped with various amounts of silicon, aluminium and zirconium.

Impurity content (wt.%)	**Unit cell parameter (Å)**	**Unit cell volume (Å^3)**	**Average crystallite size (nm)**
0	5.5788(1)	173.6(1)	69 ± 2
0.2 – Al	5.5879(3)	174.5(1)	52 ± 1
0.4 – Al	5.5871(4)	174.4(1)	44 ± 1
1 – Al	5.5845(2)	174.4(1)	45 ± 1
0.2 – Si	5.5858(2)	174.3(1)	75 ± 3
0.4 – Si	5.5815(3)	173.9(1)	61 ± 3
1 – Si	5.5771(3)	173.5(1)	58 ± 4
0.2 – Zr	5.5816(2)	173.9(1)	69 ± 1
0.4 – Zr	5.5816(2)	173.9(1)	62 ± 1
1 – Zr	5.5795(2)	173.7(1)	59 ± 1

The morphology of the oxide powders obtained at 873 K was further observed by SEM (**Figure 2**). The characteristic habit of tetravalent actinide oxalates, i.e. square-shape platelets [22], is mostly conserved in our samples, and is inherited from the precursors. It confirms that the presence of small amounts of impurities in the solids does not affect the pseudomorph character of the oxalate-oxide thermal conversion. One can note that when small amounts of zirconium were incorporated, an embrittlement of the platelets was observed. This latter

probably occurred during the heat treatment of the powders, through the dehydration of the precursors, then the decomposition of the organic oxalate moities into CO and CO_2 [14]. Nevertheless, such a behaviour was not observed for the sample containing 1 wt.% of zirconium, and does not appear to be directly linked with the Zr incorporation.

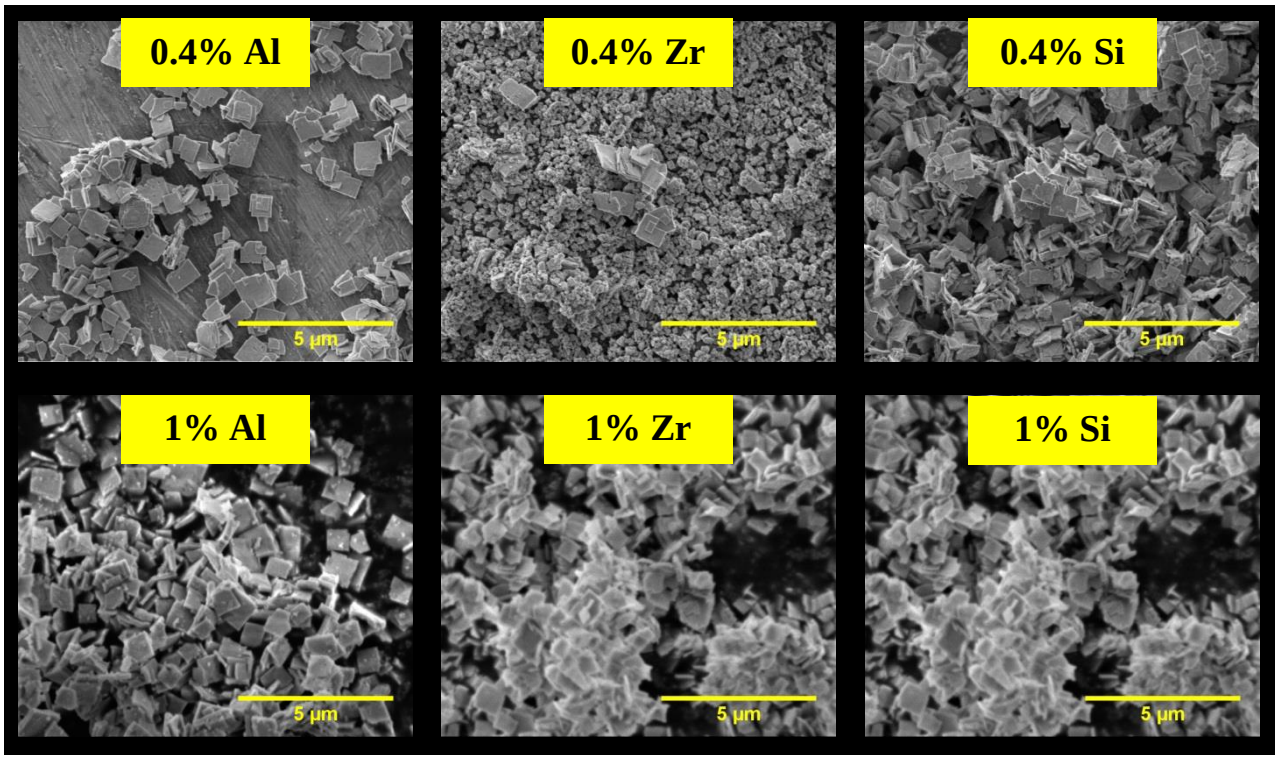

Figure 2. SEM micrographies of some oxide samples prepared after firing oxalate precursors at T = 873 K during 4 hours.

3.2 Impact of the impurities on the sintering of $Th_{0.85}Y_{0.15}O_{1.925}$

A first study was devoted to the green density of the pellets in order to evaluate the impact of the impurities on the whole ceramics fabrication process. The volume of the cylindrical green pellets was measured with a digital calliper and the mass density calculated from the unit cell parameter of pure $Th_{0.85}Y_{0.15}O_{1.925}$ ($d_{th.}$ = 9.24 g.cm^{-3}) [6] was used as a reference to determine relative densities ($d_{exp.}/d_{th.}$), expressed in %TD.

As a result, the green density of the samples containing impurities was found to be systematically equal or higher than the pure compound of reference (**Figure 3**). This effect is slightly more pronounced for the pellets containing either zirconium or silicon. Also, a maximum green density was obtained around 0.4 wt.% in dopant, up to 53 %TD for zirconium. This result can be linked to the SEM observations discussed above, which showed that dopants

resulted in some occasion in the crumbling of the aggregates constituting the powders, which in return increased the specific surface area. In these conditions, the packing of small grains led to higher green densities.

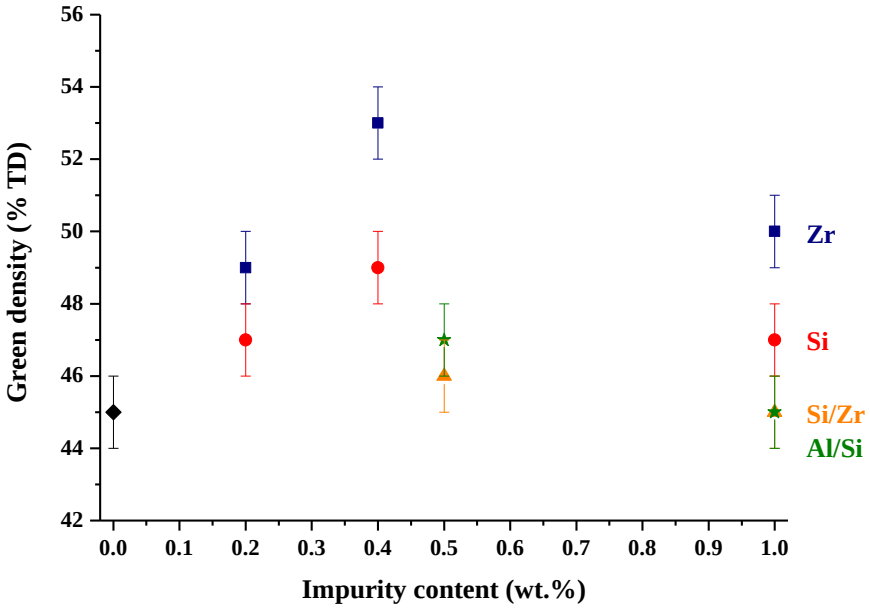

Figure 3. Variation of the green density of the green pellets versus the impurities content (expressed in wt.%, Zr - ■, Si - ●, Si/Zr - ▲, Al/Si - ★).

A dilatometric study was further undertaken in order to point out the influence of impurities over the different phenomena occurring during the heat treatment, leading from the powder compact to the sintered pellet. Overall, the linear shrinkage of all the pellets analysed followed the same trend (**Figure 4**). The densification first began through a slight contraction between 673 and 1073 K correlated with the growth of the crystallites composing the grains, as well as to the elimination of residual traces of carbon following the oxalate / oxide conversion [23]. The most important part of the shrinkage then occurred in two distinct steps. The first one started approximately at 1073 K to end at about 1473-1573 K, while the second one was mostly observed above 1673 K. Such a two-step behaviour was frequently described during the sintering of oxide powders produced by oxalic precipitation and was assigned to the densification phenomena occurring first within the aggregates, then between them [6, 23, 24].

Even if all the dilatometric curves presented a similar aspect, some differences induced by the presence of impurities were observed. When only one dopant was considered (see figures S3 and S4 supplied as supplementary material), this impact was generally small. As such, in

the case of zirconium, the variations of the relative linear shrinkage remained very similar to the reference sample whatever the incorporation rate considered. In parallel, doping with aluminium resulted only in small changes, with small amounts increasing slightly the relative linear shrinkage, while contents above 0.4 wt.% tend to hinder it. The most important effect was observed for the samples doped with silicon, especially for the highest doping rates considered. Indeed, a dramatic decrease of the mechanical properties of the pellets was stated, sometimes leading them to break. In these conditions, the results coming from dilatometry experiments were hardly exploitable.

However, it is important to note that when another impurity was coupled to silicon, such deleterious effect was considerably decreased. Indeed, when Si was added jointly with Al or Zr, the pellets recovered after the heat treatment neither cracked nor broke. Nevertheless, the variation of the relative linear shrinkage remained significantly less important in the 673-1073 K range, which highlighted a delay in the densification process. Even if the curve then followed the trend previously described once the highest temperatures were reached (i.e. typically above 1573 K), the differences observed probably highlighted a difference in the sintering mechanism.

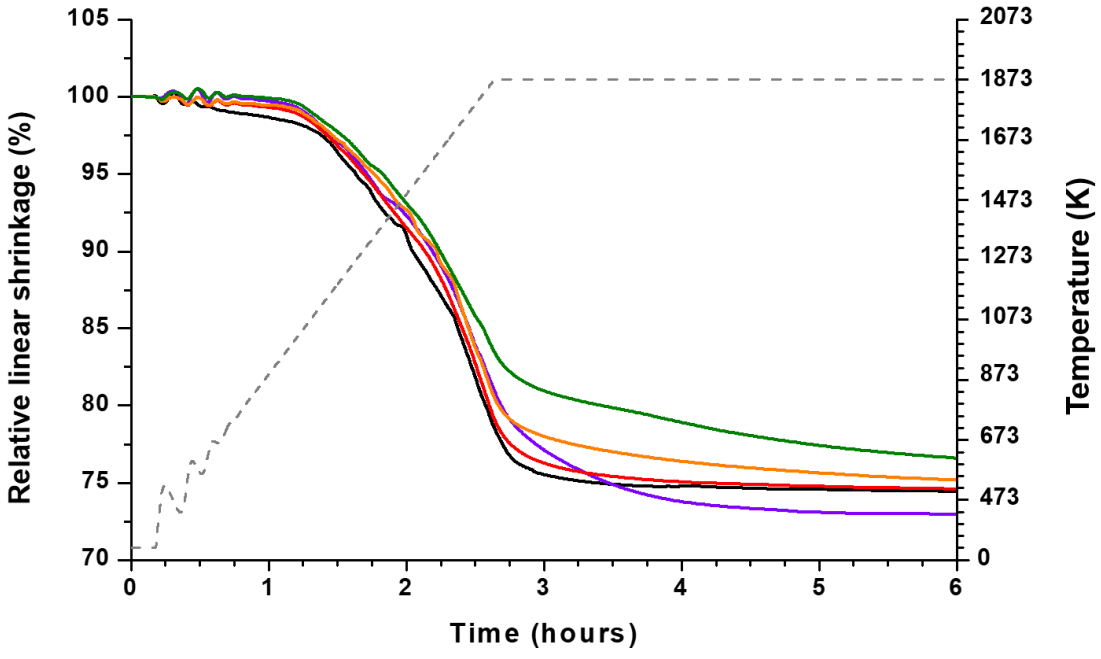

Figure 4. Evolution of the relative linear shrinkage ($\Delta L/L_0$) for $Th_{0.85}Y_{0.15}O_{1.925}$ pellets doped with a couple of impurities: 0.5 % Al/Si (red), 1 % Al/Si (purple), 0.5 % Si/Zr (orange), 1 % Si/Zr (green). The data already reported for the pure sample [6] is supplied for comparison (black).

In order to specifically point out the effect of the impurities on the microstructure of the $Th_{0.85}Y_{0.15}O_{1.925}$ pellets, a complete set of samples was sintered at 1973 K for 8 hours under air atmosphere. These operating conditions were already proved to be adapted to meet the specifications required to use the electrolyte ceramics in extreme environment (i.e. submicrometric grain size, d > 97 %TD) [6]. The density of the sintered pellets was then determined by geometrical measurements, while the average grain size was obtained through image analyses following SEM observations (**Table 3**). Sintered pellets were first polished using a 1 µm diamond spray. Grain boundaries were revealed by thermal etching at 1573 K, which did not alter the microstructure of the samples. Several images (typically 4 to 8) were then recorded and processed using successively ImageJ and Gimp softwares [25] in order to determine the average grain size. Populations of around 1000 grains were considered, leading to a relative discrepancy around 2 % [26]. Finally, the equivalent disc diameter was determined for each operating condition with the ImageJ software, using the tetrakaidecahedral grain model established by Coble [27].

Table 3. Average grain sizes and relative densities determined for the pellets prepared after sintering at 1973 K for 8 hours.

Impurity	Content (wt.%)	Average grain size (nm)	Relative density (%TD) *
None	---	710 ± 120	97
Al	1	1270 ± 20	96
	0.4	590 ± 110	97
	0.2	520 ± 10	99
Si	1	Broken	
	0.4	605 ± 20	97
	0.2	595 ± 50	98
Zr	1	420 ± 15	95
	0.4	450 ± 20	96
	0.2	475 ± 20	96
Al/Si	0.5	565 ± 20	92
	1	675 ± 40	89
Si/Zr	0.5	640 ± 10	75
	1	540 ± 65	94

** Uncertainty attached to the relative density : ± 1%*

From a general point of view, the pellets prepared from powders incorporating only one doping element reached relative densities typically in the 95-99%TD range. As such, they mostly reach the target in terms of specifications. Nevertheless, the lowest density values were systematically associated to the highest impurities contents (i.e. 1 wt.%), that even led the pellet to break in the case of silicon. Similarly, the sintering capability was found to decrease significantly when couples of dopants were tested, with values as low as 75 %TD. In the same time, the incorporation of impurities was not found to impact significantly the average grain size, which remained systematically around 0.5-0.6 µm, i.e. slightly lower than the pure sample (0.7 µm). Only the sample doped with 1 wt.% in aluminium presented an increased grain growth, with an average grain size close to 1.2 µm.

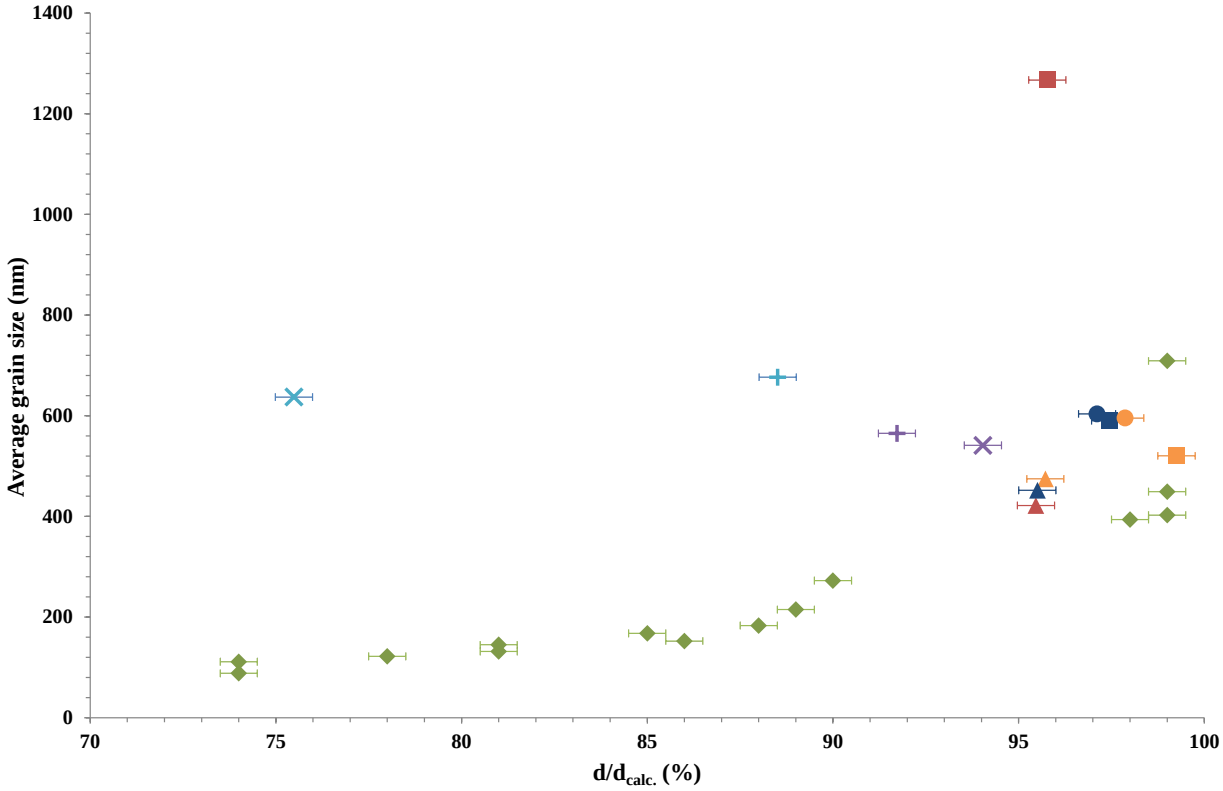

Figure 5. Comparison of the data obtained for doped materials with the sintering map of pure $Th_{0.85}Y_{0.15}O_{1.925}$ (represented by green diamonds). Symbols : Al - □ ; Zr - Δ ; Si - ○; Al/Si - + and Si/Zr - ×. Colors : orange – 0.2 wt.%, dark blue – 0.4 wt.%, red - 1 wt.%; and for impurities couples : light blue – 0.5 wt.% and purple - 1 wt.%).

As a result, the samples doped with a single impurity mostly followed the trend of the sintering trajectory built for pure $Th_{0.85}Y_{0.15}O_{1.925}$ [6] (**Figure 5**). The incorporation of aluminium and zirconium then did not impact drastically the final microstructure of the

ceramics, even if the density and grain size values were generally slightly below those of pure samples. The impurities then probably contribute in a small extent to the solute drag effect associated with the presence of yttrium [6], leading to a limited impact on the grain growth kinetics. Conversely, the microstructure was more deeply modified when dealing with couples of impurities. Even if the grain size remained submicrometric, the pellets remained poorly densified, which precludes their use as electrolytes for liquid sodium applications.

3.3 Impact of the impurities on the electrical properties of the ceramics

In order to evaluate the impact of impurities on the electrical properties of $Th_{0.85}Y_{0.15}O_{1.925}$, impedance spectroscopy measurements were undertaken on samples doped with silicon and/or zirconium, using the protocol previously employed for pure samples [8].

The Nyquist diagrams collected generally presented the same aspect than pure electrolytes, with a first arc spreading on wide range of frequencies (typically from 20 MHz to 1 kHz) and a second at lowest values (1 kHz – 0.1 Hz) but with much larger impedances, accounting for the electrode contribution. As a matter of example, the Nyquist diagrams collected for Si-doped samples sintered at 1873 K for 8 hours are gathered in **Figure 6**. The results previously obtained for the pure reference sample prepared in the same conditions are also provided for comparison purpose.

Experimental data were further modelled using the equivalent circuits method in order to extract characteristic conductivity values (**Table 4**). Such a mathematical treatment revealed the existence of two contributions within the first arc. The first one is associated to a capacitance ranging from 10^{-12} to 10^{-11} F, which is characteristic of the bulk material. The other one, with a capacitance of about 10^{-9} F, accounts for blocking phenomena. It is important to note that such a signal for blocking was absent from the data collected from the pure sample of reference. Knowing that the very high density of the materials precludes any significant contribution from the pores [6], the additional arc is then directly related to the contribution of grain boundaries. As such, its apparition concomitantly to the insertion of dopants could be the proof of the partial segregation of the impurities towards the grain boundaries. Indeed, previous studies on $Zr_{1-x}Y_xO_{2-x/2}$ systems underlined that impurities concentration was generally higher within the grain boundaries than in the bulk [28-30]. The formation of secondary phases (e.g. ZrO_2 or SiO_2 precipitates) would then induce an insulating effect increasing the blocking character of the

grain boundaries. Nevertheless, SEM observations did not evidence any precipitate, at least at the micron scale or slightly below. The precipitation of impurities then should occur as nanometric layers surrounding the grains, or segregation could only consists in the enrichment of doping elements within the grain boundaries.

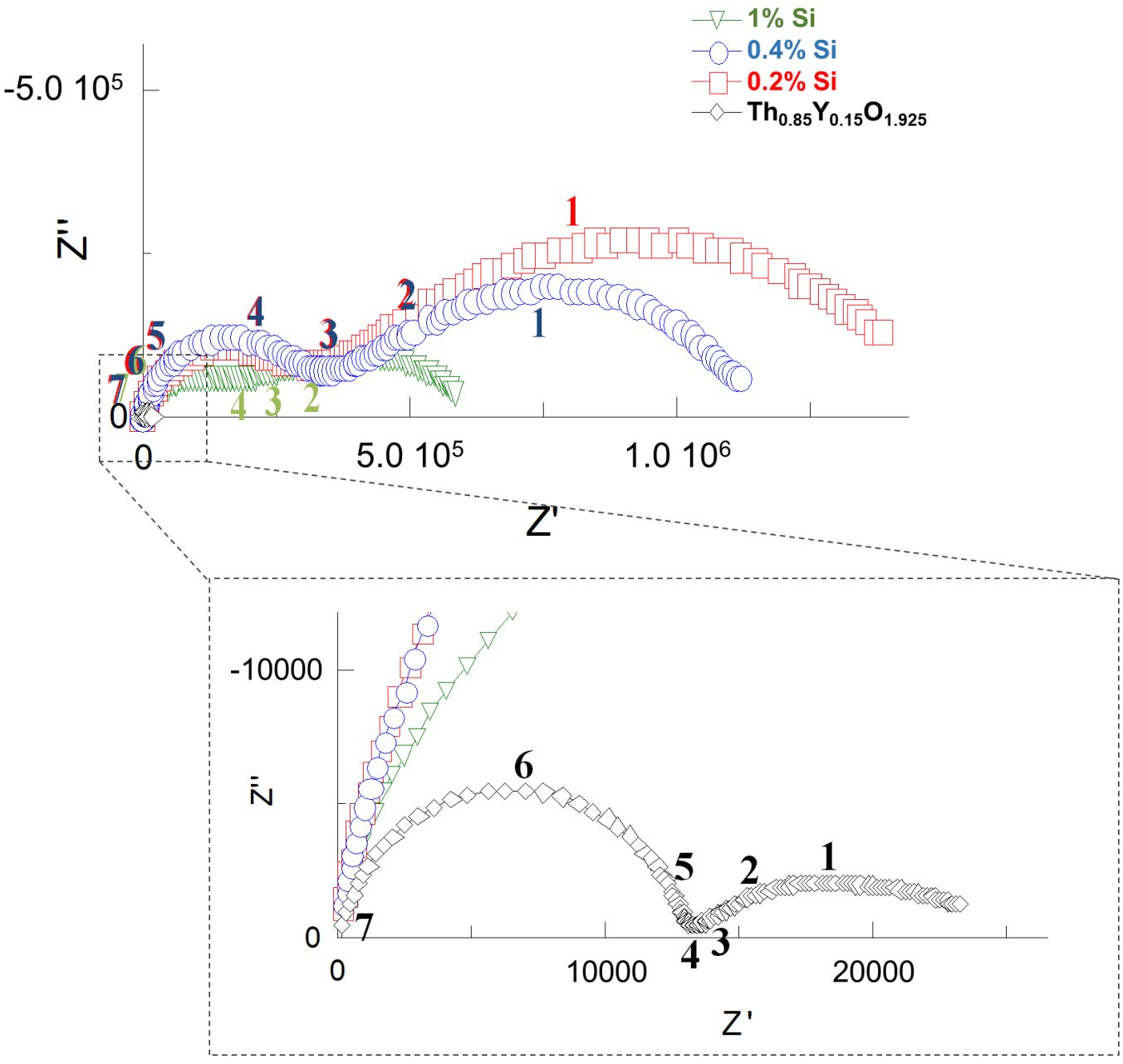

Figure 6. Nyquist diagrams collected at 773 K for Si-doped and pure $Th_{0.85}Y_{0.15}O_{1.925}$ samples sintered at T = 1873 K for 8 hours: full diagrams and focus on the high frequency domain.

Table 4. Conductivity values (expressed in $S.m^{-1}$), measured at T = 773 K, associated with the bulk material and grain boundaries contributions for Si- and Zr-doped samples sintered at T = 1973 K for 8 hours.

Impurities (wt.%)	**Silicon**		**Zirconium**	
	Bulk	Grain boundaries	Bulk	Grain boundaries
0.0	3.5×10^{-3}	/	3.5×10^{-3}	/
0.2	1.1×10^{-4}	9.6×10^{-5}	1.4×10^{-4}	1.8×10^{-4}
0.4	9.3×10^{-5}	2.5×10^{-4}	1.5×10^{-4}	2.6×10^{-4}
1.0	1.1×10^{-4}	2.3×10^{-4}	3.3×10^{-3}	3.5×10^{-4}

Whatever the nature and the content of impurities tested, the bulk conductivity was found to be significantly lower than that of the pure sample of reference, except for the compound doped with 1 wt.% of zirconium. As such, the ratio between the bulk conductivity of pure and doped materials was generally found between 25 and 40 depending on the sintering conditions considered. Such a difference supports the incorporation of silicon and zirconium within the fluorite lattice of $Th_{0.85}Y_{0.15}O_{1.925}$, in good agreement with XRD results. On this basis, if silicon is inserted in interstitial positions in the lattice, it can create thorium vacancies as illustrated by the following quasi-chemical reactions (in the Kröger-Vink notation):

$$SiO_2 = Si_i^{\bullet\bullet\bullet\bullet} + 2\,O_O + V_{Th}'''' \qquad (1.)$$

where i, O, Th subcripts account for interstitials, O and Th position in the lattice, V for vacancy, $^{\bullet}$ and $'$ for positive and negative effective charge, respectively.

Since the material contains oxygen vacancies resulting from Y doping, they can further react with thorium vacancies, leading to lattice annihilation :

$$2\,V_O^{\bullet\bullet} + V_{Th}'''' = 0 \qquad (2.)$$

Hence, silicon insertion in intertistial sites might lower the bulk conductivity by eliminating two oxygen vacancies for each silicon atom. A similar reasoning for aluminium atoms in insertion would lead to the elimination of one oxygen vacancy. Nevertheless, based

on the variation of the conductivity previously reported between $Th_{0.99}Y_{0.01}O_{1.995}$ and $Th_{0.85}Y_{0.15}O_{1.925}$ [8], the consumption of the vacancies by Si or Al cannot account completely for the dramatic decrease of the conductivity observed herein. Moreover, this explanation could not stand for Zr-doped samples, which exhibit a similar decrease in the conductivity, but where tetravalent zirconium is likely to substitute thorium on the cationic positions. Hence, doping elements could contribute to the formation of complex clusters with oxygen vacancies or modifiy lattice strain [31], which can in turn decrease the conductivity.

Also, the bulk conductivity remained in the same order of magnitude whatever the amount of dopant incorporated. This could be the sign of a saturation effect for doping rates higher than 0.2 wt.%, both for zirconium and silicon. Such a saturation effect was already described by Rajendran *et al.* [32], and could lead to the precipitation of a secondary phase, for example at the grain boundaries.

Nevertheless, the conductivity associated with the grain boundaries remained in the same order of magnitude than that of the grains themselves. It is important to recall that this contribution was absent from the pure sample of reference and comes from the blocking effect generated by the incorporation of impurities. On this basis, the specific conductivity of the grain boundaries should be very low, as it is defined as:

$$\sigma_{gb}^{sp} = \frac{L}{R_{gb}A} \cdot \frac{\delta_{gb}}{d_g} \approx \frac{L}{R_{gb}A} \cdot \frac{C_{bulk}}{C_{gb}} \qquad (3.)$$

where C_{bulk} and C_{gb} are the capacitances of the bulk and the grain boundaries, respectively, R_{gb} and δ_{gb} are the total resistance and the thickness of the grain boundary, d_g is the average grain size, L is the length of the sample, and A its cross-section [33].

If one considers a grain boundary thickness of about 1.5 nm, the calculated specific conductivity of the grain boundary is two orders of magnitude lower than the bulk, reflecting the importance of blocking elements in the grain boundary. It is then similar to acceptor-doped ZrO_2 or CeO_2 as mentioned by Guo *et al.* [33].

From the measurements performed at different temperatures, it was also possible to assess the activation energy values associated with both the bulk and the grain boundary conductivities using the Nernst-Enstein relation [34, 35] :

$$\sigma \times T = A \times e^{(-\frac{E_A}{kT})} \quad (4.)$$

The results obtained for the different samples studied, either in terms of chemical composition and of sintering conditions, are showed in **Table 5**.

The impact of impurities on the activation energy attached to bulk conductivity appeared to be correlated with the doping element. Indeed, while the incorporation of silicon did not modify the E_A value compared to pure sample (typically around 1.2 eV), adding zirconium always led to a small but constant increase of E_A. Moreover, such results were obtained whatever the sintering conditions considered. This difference could probably be explained by the difference in the ionic radii of the dopants and their coordination. Indeed, zirconium can adopt an eight-fold coordinance that is compatible with that of thorium in the ThO_2 lattice. Then, it could be directly incorporated in the cationic site and increase the lattice strains already generated by the presence of yttrium, which impacts the $Y\text{-}V_O$ interaction. Such an effect of the ionic radius on the interactions between defects and vacancies has already been evidenced by Kilner [36] and could explain the increase of the activation energy observed for Zr-doped samples [35]. Conversely, silicon does not form oxides with fluorite-type structure analogous to ThO_2. Nevertheless, as previsouly discussed, the small size of silicon (0.40 Å in 6-fold coordinance [12]) could allow its insertion in the $Y_M\text{-}V_{Ö}$ defect, preferably to its insertion on the interstitial sites, as stated above, and precludes the displacement of the vacancy. Hence, Si-doping could decrease the number of oxygen vacancies without affecting the activation energy.

Conversely, activation energies associated with the grain boundaries contribution did not follow a clear trend versus the doping elements contents. One can note that E_A values still remained systematically below the one reported for $Th_{0.99}Y_{0.01}O_{1.995}$ (1.7 eV when using similar sintering conditions, which was about 0.4 eV higher than the activation energy determined for the bulk) [8]. In this compound, the existence of blocking phenomena at the grain boundaries was assigned to a blocking effect evidenced by the lack of conductivity of the grain boundary [37] rather than to the presence of uncontrolled impurities (silicon in particular). The comparison of both data sets, *i.e.* samples with low yttrium content doping and high purity [8] versus high Y-doping and controlled impurities (this study), now backs up such an hypothesis.

Indeed, silicon even at high contents does not increase the activation energy of the grain boundaries. As such, it is more likely to decrease the efficient section for the passage of the

conducting species rather than to hinder their mobility. According to Guo *et al.* this effect could be linked to the contribution of insulated phases covering the grains [33]. In our samples, the presence of impurities led to decrease in the conductivity, even if their concentration had almost no influence in the range tested. On this basis, a saturation of the conductivity probably exists due to a complete coverage of the grains by some insulated secondary phases [28].

One the other hand, zirconium increases the activation energy assigned to the grain boundaries in the same trend than for the bulk. Then, it could be assumed that similar lattice strains exist in the grain boundaries and the bulk, due to similar Zr contents. Nevertheless, a part of zirconium is still expected to precipitate as a secondary phase at the grain boundaries and limit current flow.

Table 5. Activation energies (expressed in eV) attached to the conduction of bulk and grain boundaries as a function of the sintering conditions applied and the doping rate in silcon or zirconium.

	Impurities (wt.%)	**1873 K – 8h**		**1973 K – 8h**		**1973 K – 2h**	
		Bulk	**Grain boundaries**	**Bulk**	**Grain boundaries**	**Bulk**	**Grain boundaries**
	0	1.2	/	1.2	/	1.2	/
Si	**0.2**	1.2	1.2	1.2	1.2	1.2	1.2
	0.4	1.4	1.2	1.2	1.4	1.2	1.4
	1	1.3	1.3	1.2	1.2	1.2	1.2
Zr	**0.2**	1.4	1.5	1.5	1.5	1.5	1.6
	0.4	1.3	1.2	1.5	1.6	1.3	1.3
	1	1.2	1.3	1.5	1.2	/	/

Attached uncertainty: ± 0.1 eV

3.4 Liquid sodium corrosion tests of doped materials

Impurities are frequently reported to be harmful towards the resistance of ceramic electrolytes towards corrosion in liquid sodium [9, 10]. In order to evaluate this effect, $Th_{0.85}Y_{0.15}O_{1.925}$ pellets doped with 0.2 – 1 wt.% zirconium or silicon were submitted to liquid

sodium corrosion tests, following the protocol already described in details in our previous publication [8]. One must note that for the samples doped with 1 wt.% Si, only a fragment of pellet was used, consequently to the mechanical fragility inherited from sintering. The experiments were conducted at 773 K during 200 to 500 hours, on samples sintered at 1873 K or 1973 K for 8 hours. In these conditions, the oxygen content in the sodium was estimated to be about 70-80 ppm. The pellets were further observed by scanning electron microscopy, either of the surface or after fracture, to qualitatively assess the evolution of their microstructure. **Table 6** offers a summary of the different tests performed while **Figures S5 and S6** provide an overview of the SEM observations.

Table 6. Summary of corrosion tests performed at T = 773 K in liquid sodium.

Impurity	wt.%	Sintering conditions	Test duration (h)	SEM observations
Zr	0.2	1873 K – 8h	200	Surface
	0.4	1873 K – 8h	500	Surface / Fracture
		1973 K – 8h		
	1	1873 K – 8h	500	Fracture
		1973 K – 8h		
Si	0.2	1873 K – 8h	200	Surface
	0.4	1873 K – 8h	500	Fracture
		1973 K – 8h		
	1	1873 K – 8h	500	Fracture
		1973 K – 8h		

As the microstructural characteristics of the pellets did not evolve strongly between the two sintering conditions tested, neither density nor grain size were found to modify the behaviour in liquid sodium. This also means that the speciation of the impurities remained unchanged, and that no significant segregation of either silicon or zirconium towards grain boundaries occured when raising the sintering temperature from 1873 to 1973 K. Consequently, the results will be presented in this section without discriminating the sintering conditions.

If the initial microstructure of the pellets did not modify their chemical durability in the conditions tested, the nature and the amount of doping elements incorporated in the ceramics strongly impacted their behaviour in liquid sodium. For the lowest incorporation rate considered (i.e. 0.2 wt.% of silicon or zirconium), the surface of the pellets did not show any evidence of macroscopic corrosion, such as additional cracks or porosity. Only residual traces of sodium were observed when working with silicon. When higher doping rates were considered, the surface of the samples systematically appeared to be fragilized after corrosion in liquid sodium. This effect is illustrated by the numerous cracks observed at the surface of the ceramics (**Figure** 7).

After corrosion tests, the pellets were also fractured in order to observe the morphology of the cleavage fracture, as well as the penetration of sodium within the bulk. As such, the samples doped with zirconium behave similarly with pure samples. Indeed, a clear mark was observed on the micrographs, which delimitates two distinct zones of the microstructure. The outer layer is characterized by intergranular fracture, while the inner region exhibits transgranular fracturation. Such a clear demarcation evidences the penetration of liquid sodium in the samples, most likely through grain boundaries. For a weigth loading of 0.4 wt.% in zirconium, the penetrated depth reached about 110 µm after 500 hours, corresponding to a penetration rate close to 0.2 $\mu m.h^{-1}$. Owing to the uncertainties attached to this value, which was only evaluated visually on a limited zone of the sample, it could be compared to that determined for pure materials, *i.e.* 0.5 $\mu m.h^{-1}$. Zirconium then does not impact significantly the corrosion process nor enhance the corrosion rate in liquid sodium. As XRD and impedance spectroscopy measurements led to conclude that part of the zirconium is probably precipitated as a secondary phase at the grain boundaries, this means that such a phase should be stable regarding to corrosion in liquid sodium, at the least on the time scale of our experiments.

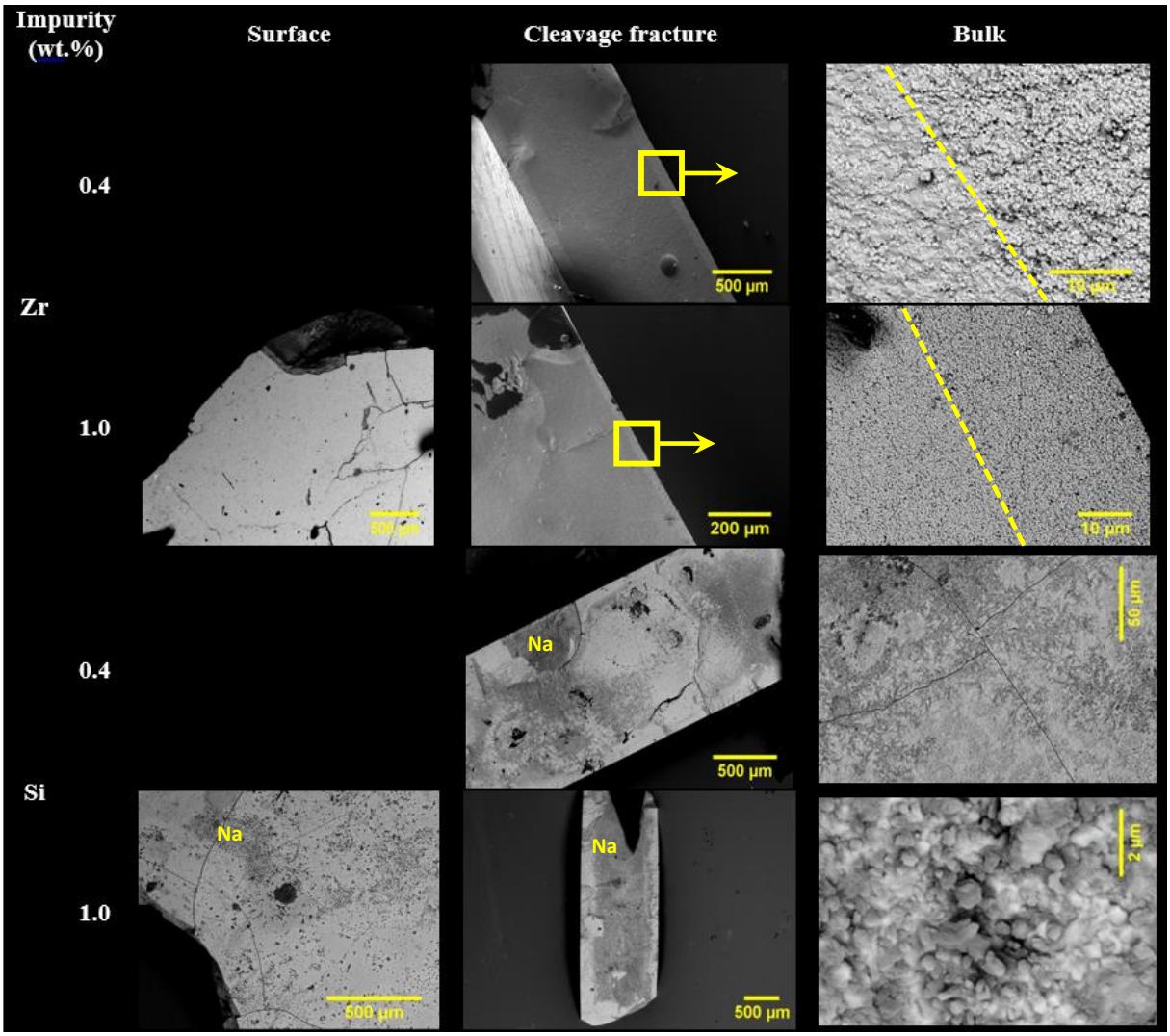

Figure 7. SEM micrographs of $Th_{0.85}Y_{0.15}O_{1.925}$ doped with silicon or zirconium after corrosion tests in liquid sodium at 773 K for 500 hours.

Conversely, the SEM micrographs collected from samples doped with silicon and tested in liquid sodium for 500 hours revealed a penetration of sodium in the whole thickness of the pellet, either for silicon contents of 0.4 and 1 wt.%. Consequently, the fracture habit was mostly intergranular, and was accompanied by the mechanical embrittlement of the pellets (or pellets fragments). Numerous cracks, already spotted at the surface, are also observed within the samples. For the highest silicon incorporation rate (i.e. 1 wt.%), the inner part of the pellet even appeared to be covered by sodium. The darkest zones observed by SEM were associated with metallic sodium that further reacted with air to form Na_2CO_3 and NaOH. These micrographs then confirmed a massive in-depth sodium penetration in the sample, and thus the very harmful effect of the silicon incorporation.

In addition to corrosion tests and SEM observations performed on Si- and Zr-doped samples, thermodynamics calculations were undertaken to assess the potential formation of ternary oxides as secondary products of the corrosion reaction, such as:

$$MO_y + Na_xO_z \rightarrow Na_xMO_{z+y} \quad (M = Th, Si, Zr) \qquad (5.)$$

The Gibbs free energies were calculated using the HSC Chemistry 5.1 software at T = 773 K, to account for the conditions of the corrosion tests. Na_2ThO_3 data were estimated from the Gibbs free energy of formation reported by Dash *et al*. [38]. In all the cases considered, the ΔG_R° value was found to be negative, meaning that the formation of such ternary oxide is thermodynamically favored. Moreover, adding impurities to the samples led Na_2SiO_3 and Na_2ZrO_3 to form preferentially compared to Na_2ThO_3. This could favor the diffusion of the sodium at the grain boundaries and enhance the fragility of the pellets, at least for samples doped with silicon.

Table 7. Calculated Gibbs free energies assigned to the formation of Na_2MO_3 (M = Th, Si, Zr) from oxides at 773 K and associated dissolved oxygen contents required for the formation of ternary oxides.

Equation		$\Delta G_{f,ox}$ (kJ.mol^{-1})	$X_0^{Na,sat}$ (µg.g^{-1})
$SiO_2 + Na_2O \rightarrow Na_2SiO_3$	(6.)	- 230	3.6×10^{-13}
$ThO_2 + Na_2O \rightarrow Na_2ThO_3$	(7.)	-79	6.1×10^{-3}
$ZrO_2 + NaO_2 \rightarrow Na_2ZrO_3$	(8.)	-169	5.1×10^{-9}

We further determined the oxygen content dissolved in the liquid sodium that is required to form the ternary oxides. To do so, the oxygen activity at the formation equilibrium of Na_2MO_3 was determined from the expression of Gibbs free energy. Since MO_2 and Na_2MO_3 are solid phases, only the activity of dissolved Na_2O differed from 1, leading to:

$$\Delta G_R^\circ - RTln\, a_{Na_2O} = 0 \qquad (9.)$$

With the hypothesis that the activity of Na_2O remained constant in liquid sodium, Henry's law leads to:

$$a_{Na_2O} = \frac{X_0^{Na}}{X_0^{Na,sat}} \quad (10.)$$

where X_0^{Na} is the oxygen content in liquid sodium and $X_0^{Na,sat}$ is the solubility of oxygen in the liquid sodium (both expressed in µg per g of sodium). This latter was determined using the empirical relation established by Noden to describe the variation of the oxygen solubility in liquid sodium between 403 and 823 K [39] :

$$\log X_0^{Na,sat} = 6.2571 - \frac{2444.5}{T} \quad (11.)$$

Considering equations (8) to (10), it was then possible to determine the threshold value beyond which Na_2MO_3 ternary oxides are expected to form:

$$ln\, X_0^{Na} = \frac{\Delta G_{f,ox}^{\circ}}{R \times T} + \log\left(X_0^{Na,sat}\right) \quad (12.)$$

The results reported in **Table 7** show that the formation of all the Na_2MO_3 compounds considered with M = Th, Si and Zr should occur even for very low amounts of dissolved oxygen, typically below 1 ppm. These values are then compatible with highly-purified nuclear-grade sodium (1-3 ppm oxygen in operation). As the oxygen concentration during the corrosion tests was estimated to be about 80 ppm, the formation of ternary oxides is then thermodynamically expected, even if their formation was not evidenced on the SEM micrographs. Once again, it argues for a limited precipitation of such phases at the grain boundaries, which still would be sufficient to weaken the material and favor the penetration of sodium in the bulk. The differences observed between samples doped with zirconium and silicon then could arise from some differences in the kinetics of formation of the ternary oxides.

4. Conclusion

The effect of various impuritites, i.e. aluminium, zirconium and silicon, on the life-cycle of $Th_{0.85}Y_{0.15}O_{1.925}$ electrolyte to be used in electrochemical oxygen sensors for liquid sodium was evaluated in this study. After firing the oxalate precursors at 873 K, all the oxide powders prepared were found to exhibit the single-phase fluorite-type structure expected for such materials, while the variation of the unit cell parameter confirmed the incorporation of the impurities in the lattice. Doping with 0.2 – 1 wt.% of impurities only slightly affected the morphology of the powders, for example by decreasing the grain size. After sintering, the effect of impurities over the microstructure of the prepared pellets also remained limited. Indeed, the relative density / grain size data fit well with the sintering trajectories established previously for pure materials. A deleterious effect, i.e. drastic decrease of the density or even pellet break, was only observed when incorporating two impurities or silicon with high contents in the material. On this basis, and keeping in mind that doping rates considered herein were willingly exaggerated compared to what should be expected from a real-life process, one can conclude that impurities should not impact the preparation of the electrolyte ceramics.

The presence of silicon and zirconium in the ceramic further modified its electrical properties, even if it remains difficult to establish a clear correlation with the doping rate probably due to a saturation effect leading to the precipitation of secondary phases. Overall, the grain conductivity was always found to decrease, in good agreement with the incorporation of Si and Zr in the lattice. In the case of zirconium, this effect was due to the direct substitution of Th^{4+} by the smaller Zr^{4+}, thus enhancing the lattice strains. For silicon, the stabilization of the Y_M-$V_{Ö}$ defect leading to block the vacancies was more likely suspected. More importantly, impedance spectroscopy revealed a strong modification of the Nyquist diagram compared with the pure sample used as reference, which evidenced that impurities partially migrated towards grain boundaries during the sintering step.

Finally, the corrosion tests undertaken in liquid sodium at 773 K showed that the pellets were fragilized by the presence of silicon at any tested content, on the one hand, or by high zirconium contents, on the other hand. This weakening effect was associated with the penetration of sodium through the grain boundaries, possibly through the formation of Na_2MO_3 ternary oxides. Even if the thermodynamic calculations showed that such phases should form for all the M elements considered (i.e. Si, Zr or Th), silicon clearly presented the most deleterious effect, likely because of kinetics considerations.

From a general point of view, silicon then seems to be the most harmful impurity that should be especially checked during the fabrication processes. For the other elements studied contents as high as few tenth ppm are not expected to significantly affect neither the properties of the ceramics, nor their chemical durability in operating conditions.

Acknowledgments. The authors would like to thank Sandra Ollivier and Florent Bernard for performing the synthesis of the samples, Adel Mesbah for PXRD data refinement, as well as Vincent Beau and Smaïl El Hannaoui for their help during corrosion experiments and SI measurements. They are also grateful to CEA for its continuous financial support. Last, but not least : welcome to the world, Jeanne !

References

[1] J.E. Kelly, *Prog Nucl Energ* **77** (2014) 240-246.
[2] L. Brissonneau, *J Nucl Mater* **423**(1-3) (2012) 67-78.
[3] E. Schouler, A. Hammou, M. Kleitz, *Mater Res Bull* **11**(9) (1976) 1137-1146.
[4] J.L. Courouau, J. Fouletier, M.C. Steil, *Electrochim Acta* **331** (2020).
[5] V. Jayaraman, T. Gnanasekaran, *J Electrochem Soc* **163**(7) (2016) B395-B402.
[6] Y. Cherkaski, N. Clavier, L. Brissonneau, R. Podor, N. Dacheux, *J Eur Ceram Soc* **37**(10) (2017) 3381-3391.
[7] M.F. Lasker, R.A. Rapp, *Z Phys Chem Neue Fol* **49**(3-5) (1966) 198-&.
[8] Y. Cherkaski, N. Clavier, L. Brissonneau, N. Dacheux, *Corros Sci* **171** (2020) 108721.
[9] J. Jung, A. Reck, R. Ziegler, *J Nucl Mater* **119**(2-3) (1983) 339-350.
[10] D. Jakes, J. Kral, J. Burda, M. Fresl, *Solid State Ionics* **13**(2) (1984) 165-173.
[11] S. Kano, E. Yoshida, Y. Hirakawa, Y. Tachi, H. Haneda, T. Mitsuhashi, *Liquid Metal Systems* (1995) 85-94.
[12] R.D. Shannon, *Acta Crystallogr A* **32**(Sep1) (1976) 751-767.
[13] M. Gabard, Y. Cherkaski, N. Clavier, L. Brissonneau, M.C. Steil, J. Fouletier, A. Mesbah, N. Dacheux, *J Alloy Compd* **689** (2016) 374-382.
[14] D. Horlait, N. Clavier, N. Dacheux, R. Cavalier, R. Podor, *Mater Res Bull* **47**(12) (2012) 4017-4025.
[15] P. Thompson, D.E. Cox, J.B. Hastings, *J Appl Crystallogr* **20** (1987) 79-83.
[16] C. Frontera, J. Rodriguez-Carvajal, *Physica B: Condensed Matter* **335**(1-4) (2003) 219-222.
[17] E.C. Subbarao, H.S. Maiti, *Solid State Ionics* **11**(4) (1984) 317-338.
[18] L. Bonato, M. Virot, T. Dumas, A. Mesbah, E. Dalodière, O. Dieste, T. Wiss, X.F. Le Goff, M. Odorico, D. Prieur, A. Rossberg, L. Venault, N. Dacheux, P. Moisy, S. Nikitenko, *Nanoscale Adv.* **2** (2020) 214-224.
[19] L. Claparede, N. Clavier, N. Dacheux, A. Mesbah, J. Martinez, S. Szenknect, P. Moisy, *Inorg Chem* **50**(22) (2011) 11702-11714.

[20] V. Tyrpekl, J.F. Vigier, D. Manara, T. Wiss, O.D. Blanco, J. Somers, *J Nucl Mater* **460** (2015) 200-208.

[21] T.V. Plakhova, A.Y. Romanchuk, D.V. Likhosherstova, A.E. Baranchikov, P.V. Dorovatovskii, R.D. Svetogorov, T.B. Shatalova, T.B. Egorova, A.L. Trigub, K.O. Kvashnina, V.K. Ivanov, S.N. Kalmykov, *J Phys Chem C* **123**(37) (2019) 23167-23176.

[22] F. Abraham, B. Arab-Chapelet, M. Rivenet, C. Tamain, S. Grandjean, *Coordin Chem Rev* **266** (2014) 28-68.

[23] J. Martinez, N. Clavier, T. Ducasse, A. Mesbah, F. Audubert, B. Corso, N. Vigier, N. Dacheux, *J Eur Ceram Soc* **35**(16) (2015) 4535-4546.

[24] D. Horlait, A. Feledziak, F. Lebreton, N. Clavier, D. Prieur, N. Dacheux, T. Delahaye, *J Nucl Mater* **441**(1-3) (2013) 40-46.

[25] C.A. Schneider, W.S. Rasband, K.W. Eliceiri, *Nature Methods* **9**(7) (2012) 671-675.

[26] A. Maitre, D. Beyssen, R. Podor, *Ceram Int* **34**(1) (2008) 27-35.

[27] R.L. Coble, *J Appl Phys* **32**(5) (1961) 787-&.

[28] M. Aoki, Y.M. Chiang, I. Kosacki, I.J.R. Lee, H. Tuller, Y.P. Liu, *J Am Ceram Soc* **79**(5) (1996) 1169-1180.

[29] E.J.L. Schouler, N. Mesbahi, G. Vitter, *Solid State Ionics* **9-10**(Dec) (1983) 989-996.

[30] M.J. Verkerk, A.J.A. Winnubst, A.J. Burggraaf, *J Mater Sci* **17**(11) (1982) 3113-3122.

[31] M.J.D. Rushton, A. Chroneos, S.J. Skinner, J.A. Kilner, R.W. Grimes, *Solid State Ionics* **230** (2013) 37-42.

[32] S. Rajendran, J. Drennan, S.P.S. Badwal, *J Mater Sci Lett* **6**(12) (1987) 1431-1434.

[33] X. Guo, R. Waser, *Prog Mater Sci* **51**(2) (2006) 151-210.

[34] C.M. Choudhary, H.S. Maiti, E.C. Subbarao, Defect structure and transport properties, in: E.C. Subbarao (Ed.), Solid electrolytes and their application, Springer US1980, pp. 1-80.

[35] J.A. Kilner, *Solid State Ionics* **129**(1-4) (2000) 13-23.

[36] J.A. Kilner, C.D. Waters, *Solid State Ionics* **6**(3) (1982) 253-259.

[37] M. Kleitz, L. Dessemond, M.C. Steil, F. Thevenot, *Electrically Based Microstructural Characterization* **411** (1996) 269-275.

[38] S. Dash, Z. Singh, S.C. Parida, V. Venugopal, *J Alloy Compd* **398**(1-2) (2005) 219-227.

[39] D. Noden, *J Brit Nucl Ener Soc* **12** (1973) 57-62.

Supplementary Material

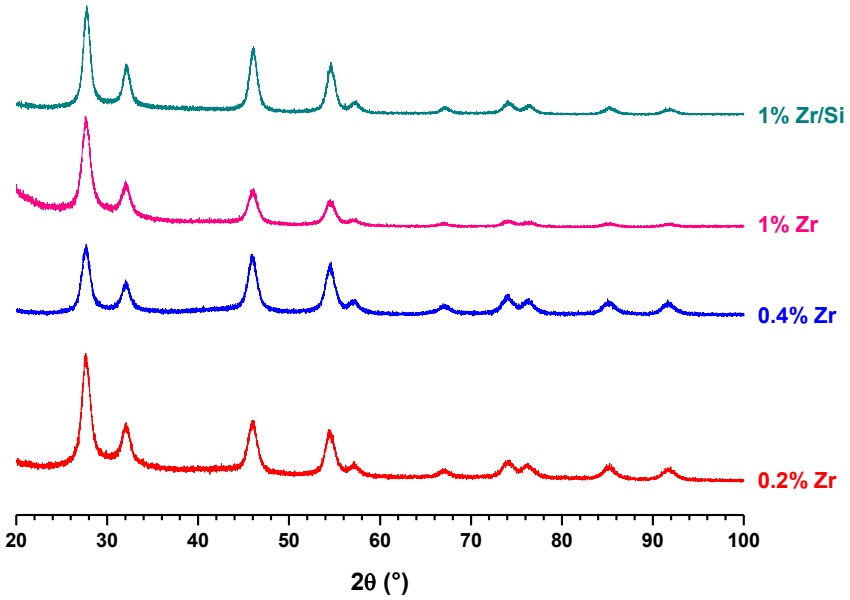

Figure S1. XRD patterns of $Th_{0.85}Y_{0.15}O_{1.925}$ doped with various amounts of zirconium.

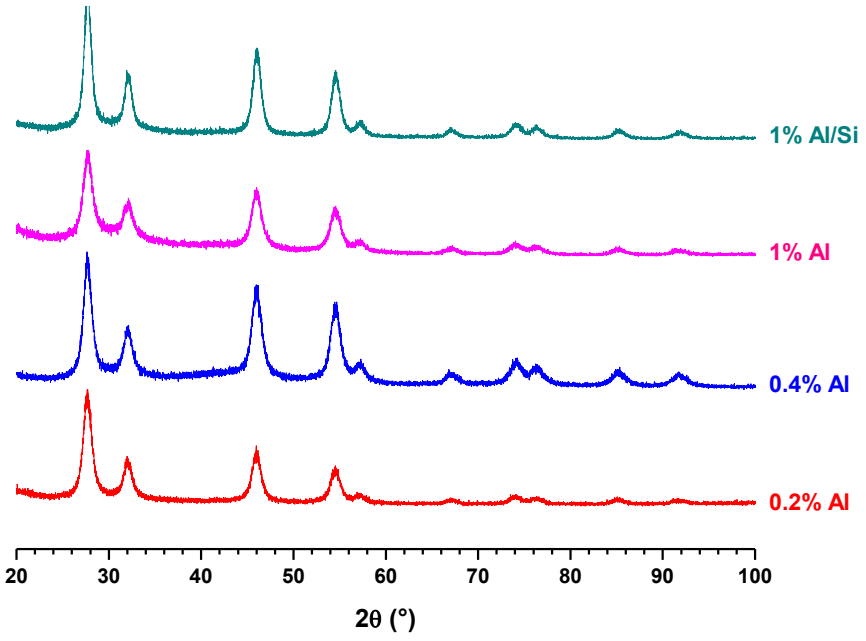

Figure S2. XRD patterns of $Th_{0.85}Y_{0.15}O_{1.925}$ doped with various amounts of aluminium.

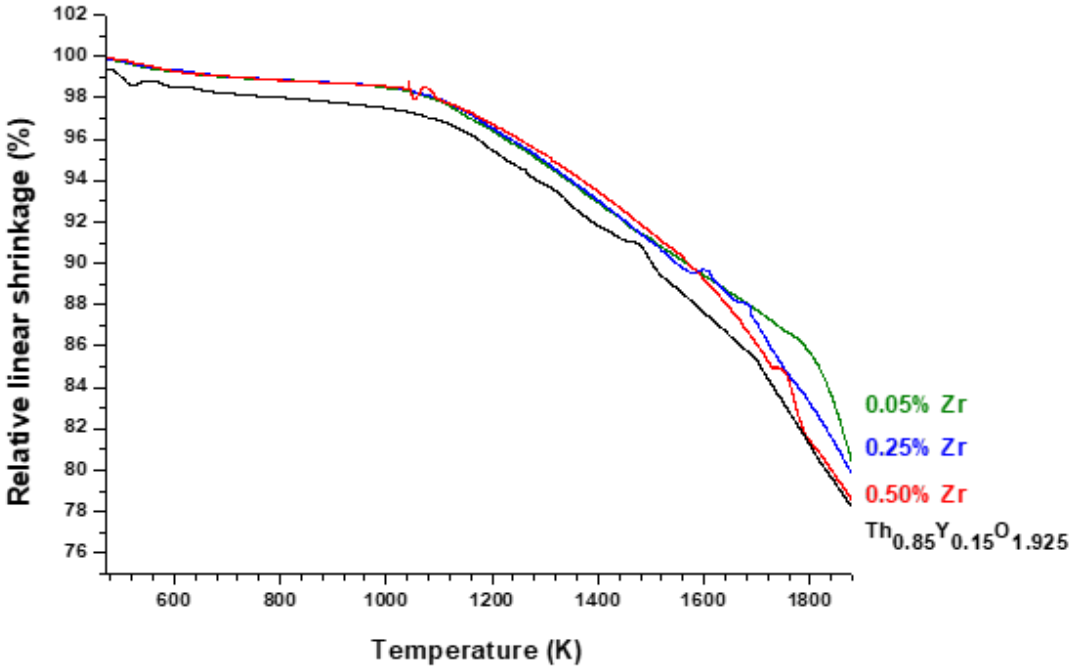

Figure S3. Dilatometric curves of $Th_{0.85}Y_{0.15}O_{1.925}$ samples doped with various amounts of zirconium.

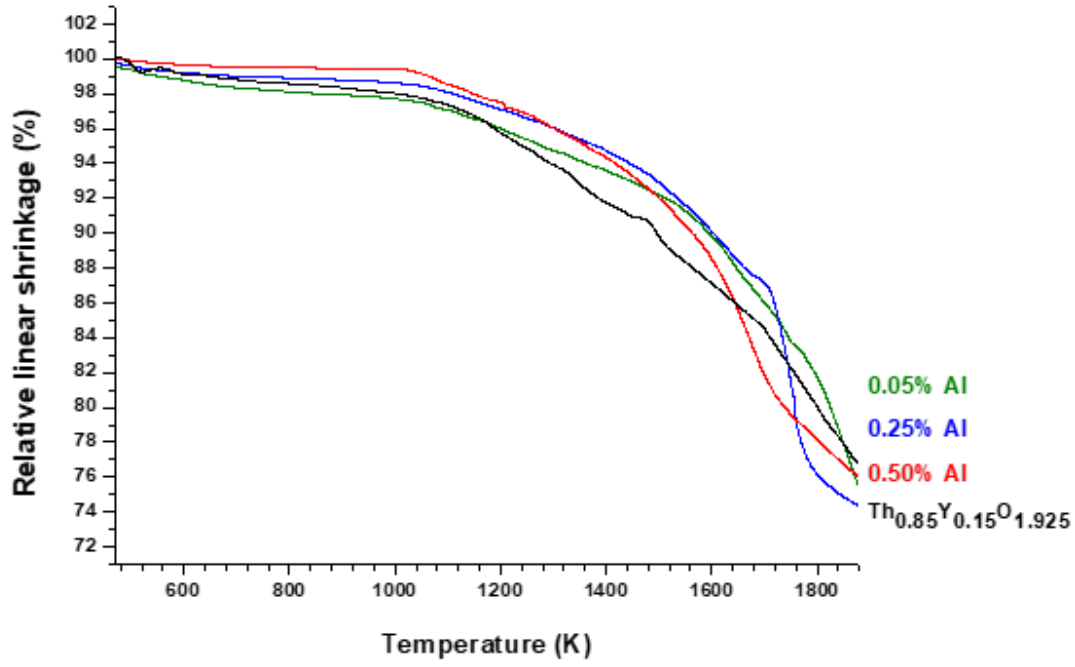

Figure S4. Dilatometric curves of $Th_{0.85}Y_{0.15}O_{1.925}$ samples doped with various amounts of aluminium.

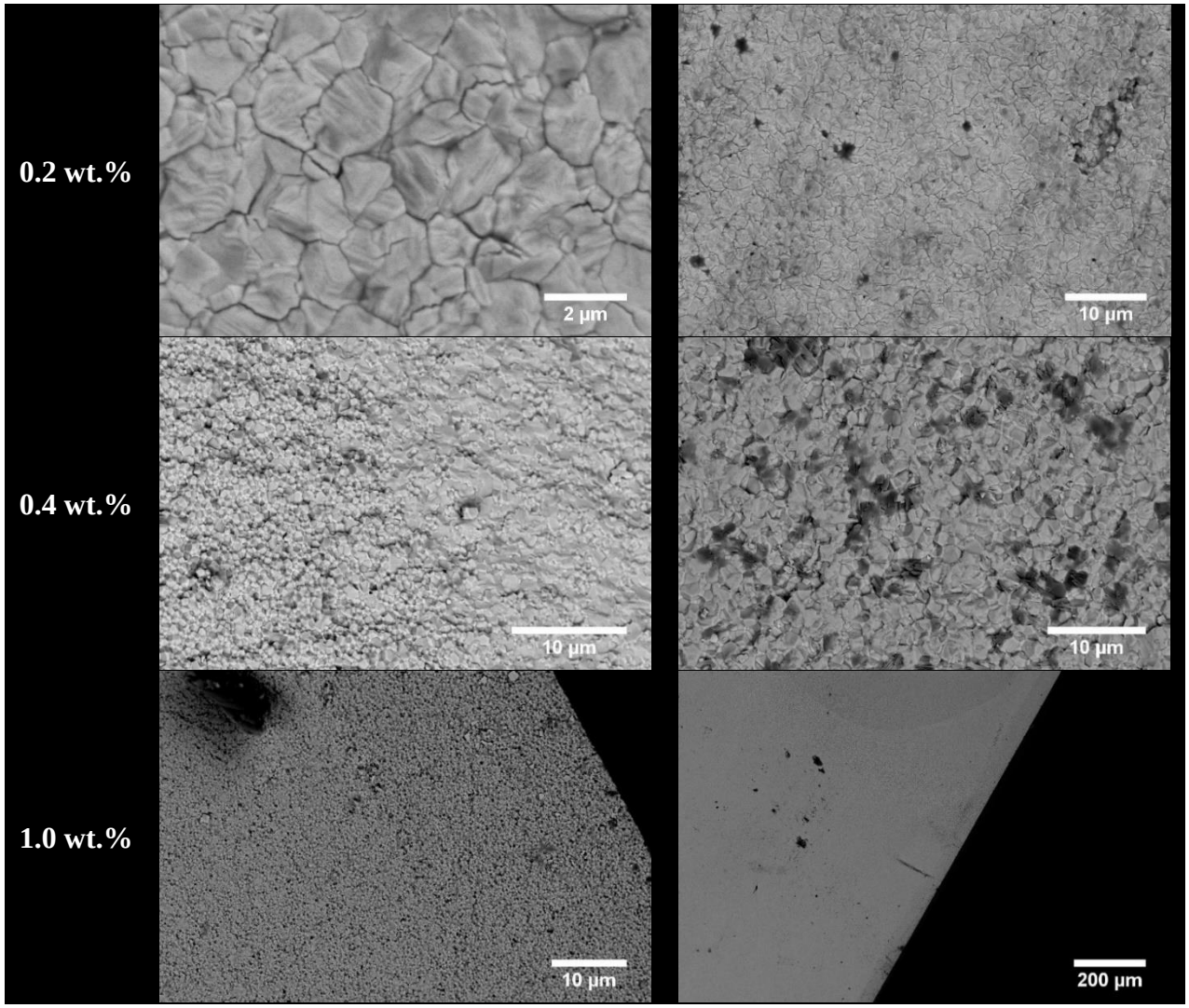

Figure S5. **Cross-section** SEM observations of $Th_{0.85}Y_{0.15}O_{1.925}$ samples doped with various amounts of zirconium, after immersion in liquid sodium at T = 500°C.

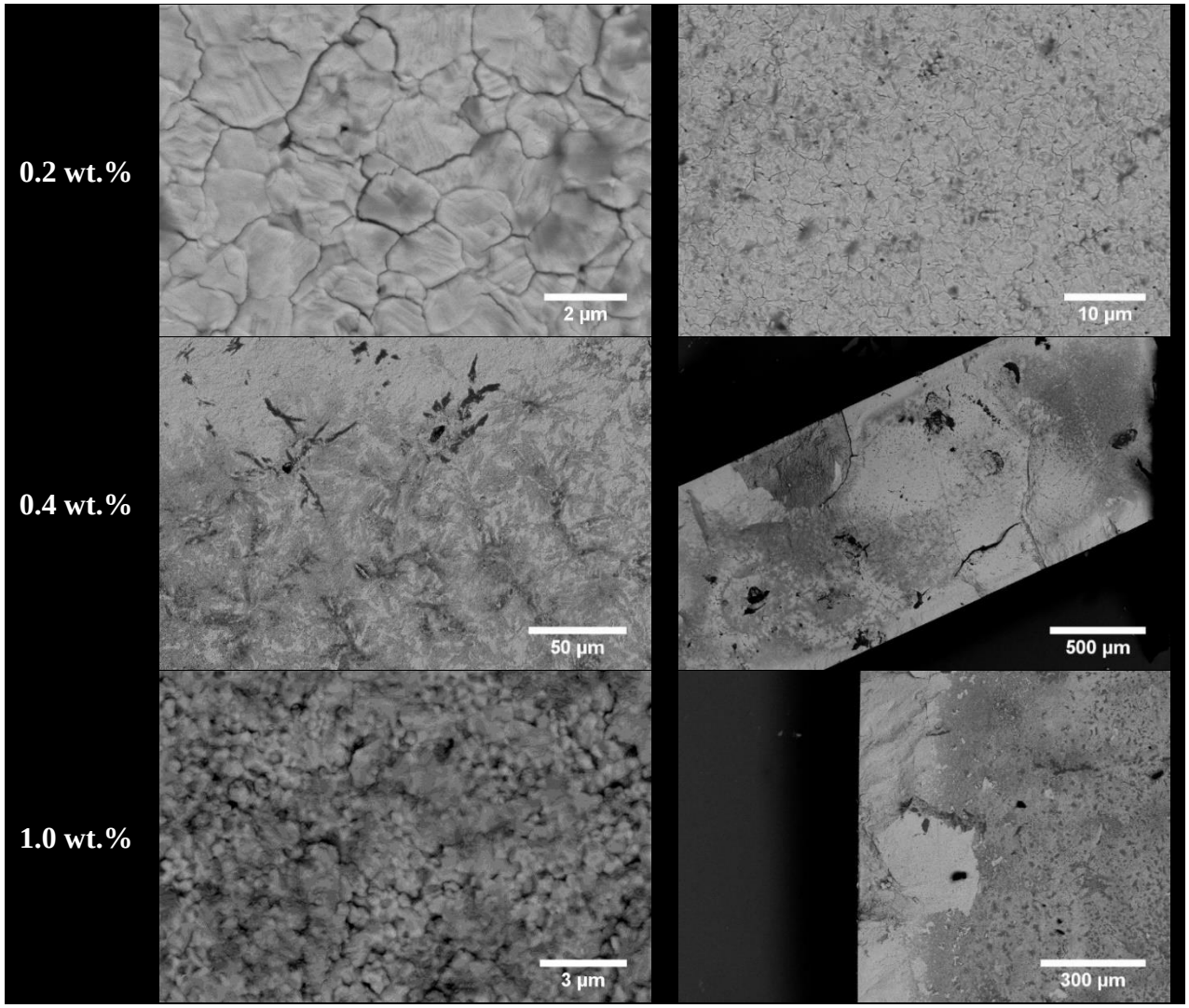

Figure S6. **Cross-section** SEM observations of $Th_{0.85}Y_{0.15}O_{1.925}$ samples doped with various amounts of silicon, after immersion in liquid sodium at T = 500°C.